

# Decarbonizing an industrial process through a combined, high-temperature CSP and sensible heat storage

A. Martín-Alcántara<sup>a,b,\*</sup>, J.J. Serrano-Aguilera<sup>c</sup>, A. Sánchez-Puerta<sup>a</sup>, J.L. Aranda-Hidalgo<sup>a,d</sup>

<sup>a</sup>*Magtel I+D+i, P.E. Las Quemadas, C/ Gabriel Ramos Bejarano, 114, Córdoba, 14014, Spain*

<sup>b</sup>*Grupo de Modelización y Sistemas Físicos (FQM-378), Facultad de Ciencias,*

*Universidad de Córdoba, Campus de Rabanales, Edif. Einstein, Córdoba, 14071, Spain*

<sup>c</sup>*Universidad de Málaga, Escuela de Ingenierías Industriales, Campus de Teatinos, s/n, Málaga, 29071, Spain*

<sup>d</sup>*Departamento de Mecánica, Escuela Politécnica Superior de Córdoba,*

*Universidad de Córdoba, Campus de Rabanales, Edif. Leonardo da Vinci, Córdoba, 14071, Spain*

---

## Abstract

Decarbonization is crucial for meeting global environmental goals by 2050 and combating climate change. The current work studies a thermal system combining CSP (solar dish) and thermal energy storage (TES) technologies aimed at reducing CO<sub>2</sub> emissions. Given the Direct Normal Irradiance (DNI) profiles of two southern Spain locations (Córdoba and Málaga), numerical simulations have been conducted to analyze the power and the energy provided by this proof of concept in three representative days of 2022 (two equinoxes and one solstice). One or several solar dishes first increase the temperature of the heat transfer fluid (HTF). Then, following a simple decision-making algorithm, the mass flow enters or bypasses a TES unit. If additional energy is required to meet a final temperature, it is supplied externally from e.g. electric sources. A sensitivity analysis has shown that four solar dishes in parallel connection, combined with a TES unit of aspect ratio  $L/D = 1.5$  (if in Córdoba) or  $L/D = 1.0$  (if in Málaga), is a suitable solution to effectively reduce the external energy consumed by the system as well as the operation cost and the environmental impact.

**Keywords:** Decarbonization, numerical simulation, solar dish (CSP), thermal energy storage (TES), high-temperature heat.

---

## 1. Introduction

The potential impact of climate change on the global environmental balance and the subsequent effects on the global social and economic issues, justify the efforts to achieve significant CO<sub>2</sub> emis-

---

\*Corresponding author

*Email addresses:* antonio.alcantara@magtel.es,  
a.martin@uco.es (A. Martín-Alcántara),  
jj.serragui@uma.es (J.J. Serrano-Aguilera),  
alvaro.sanchez@magtel.es (A. Sánchez-Puerta),  
joseluis.aranda@magtel.es (J.L. Aranda-Hidalgo)

*Preprint submitted to Energy Convers. Manag.*

*February 29, 2024*

sion reduction in the coming years. The most significant advances have been made in electricity generation, mainly due to solar photovoltaic (PV), wind energy, and concentrated solar power (CSP). However, there is still a challenge to overcome in terms of heat supply for the industry, particularly in those considered hard-to-abate sectors [1]. Similarly, renewables still account for a reduced fraction (5.6 % in 2021) of global heat generation [2]. According to Madeddu et al. [3] the replacement of fossil fuels for the industry is at the core of the 2050 climate neutrality target of the EU. Direct electrification of heat supply is supposed to be one of the most convenient strategies, but the limits of heat pumps for heat supply at high temperatures restrict the leeway of this scheme for industrial processes that require heat at temperatures higher than approximately 200 °C. It is worth noting that pumps operating above 150 °C can barely be found in the literature [4]. Since this limitation, CSP in combination with thermal energy storage (TES) becomes an ideal complement to reduce CO<sub>2</sub> emissions for such applications, especially in countries such as Spain, due to two key factors. (i) The Spanish generation mix is based on a significant share of non-fossil sources for electricity generation. As of 2022, renewable sources account for 42.2% of the energy in the Spanish grid, along with 20.3% from nuclear [5]. (ii) Furthermore, the Iberian Peninsula benefits from suitable weather and solar ra-

diation conditions [6] for the massive deployment of CSP, where the case of Andalusia can be highlighted, selecting two of its cities for the location of this study.

In that sense, solar parabolic dishes are commonly accepted as the most efficient CSP technology for the exploitation of solar energy in the range of kWCoventry and Andraka [7]. Due to their optical efficiency and the nature of the materials (e.g. Ni foam), and of course depending on the dish surface, the temperature increase can be of the order of thousands of degrees. Moreover, the possibility of deploying the dish where required is a huge advantage in reducing thermal and mechanical transport losses. Basically, the dish consists of a parabolic reflector concentrating the radiative energy of the sunlight at the focal point, where the solar receiver is installed. Concentrated radiation enters the receiver through a high-temperature glass window (e.g. quartzite). Inside the receiver, different convective-conductive heat exchange processes take place, with the aim of heating a Nickel foam, which is the heart of the solar dish. Two reference works that model the entire performance of the dish are those of Zhu et al. [8] and García Ferrero et al. [9]. Starting from an optical analysis, considering the actual dish geometry through view factors, they formulate the different thermal processes occurring inside the receiver to eventually provide the outlet temperature. Thermal

losses are also considered in both works. The main difference between the two models is the heat transfer considerations between the glass and the foam. In particular, García Ferrero et al. [9] separated on the one hand the heat exchange with the glass and on the other hand the convective heat transfer with the foam. Additional differences have been found in the heat transfer correlations used by each author. This work has been inspired by the aforementioned, but it also considers the heat balance and the source term within the glass window.

To gain flexibility, thermal energy storage has become quite popular in recent years because it represents an ideal solution to decarbonize energy systems, such as power generation on a utility scale, industry, district heating and cooling, buildings and cold chain logistics International Renewable Energy Agency [10]. Depending on the final temperature range, different TES technologies might be used. For instance, in the range 600–700 °C the most suitable strategy is latent or sensible heat storage (e.g. solid-state, molten salts and phase-change materials), which are efficient ( $\sim 90\%$ ) mature technologies with a long lifetime. Thermochemical systems can deal with higher temperature ranges, say 500–900 °C, but their efficiency is lower ( $\sim 50\%$ ) and the level of technological maturity is still limited. Furthermore, the useful lifetime is considerably shorter International Renewable Energy Agency [10]. To

improve the operation of concentrated solar power plants (CSPs), TES is without a doubt the most suitable solution. Consequently, new and promising TES materials with different configurations are being investigated to minimize costs and increase operating temperatures in thermal applications Pascual et al. [11]. Two main categories can be proposed for TES configurations in CSP plants. If the storage medium is a fluid (e.g., molten salts [12–15] or phase change materials [16–18]) it can be referred to as active storage. Otherwise, if a solid is used to store sensible heat, it is considered passive. Each of these configurations has its own advantages and drawbacks (see [11], but this work is focused on the latter, and more particularly on packed-bed systems, because solids are generally cheaper and can operate at higher temperature ranges and higher heat transfer rates. As an example, Tiddens et al. [19] used porous ceramic bricks as a passive storage system at the Jülich solar tower facility. Typical filler materials for solid TES are sand or concrete Pascual et al. [11], John et al. [20], Villarroel et al. [21], although rocks are also a valid solution [22]. Carbon blocks [23] are becoming a promising alternative [24, 25], and this will be the TES strategy adopted throughout this work.

Therefore, the objective of this paper is to analyze the operation of a thermal cycle supplying high-temperature heat for the decarbonization of an industrial activity (e.g. chemical, cement,

steel, electrolysis processes, etc.[26–28]) through a simple unsteady mathematical model that integrates CSP (solar dishes) and (carbon blocks) TES technologies. The primary objective is to analyze and understand the overall performance of the cycle, gaining valuable insight into the configuration and design of the CSP & TES systems. Furthermore, the study aims to estimate the timescales involved in the processes, which is important for the practical implementation of the CSP-TES system, ultimately responding to the registered utility model **AAABBB**. The work is summarized as follows. First, the operation of the cycle and its elements are summarized. Sect. 3 describes the mathematical models for the solar dish, for the TES, and for the combined solution. Next, the numerical results obtained with the mathematical models are shown and discussed in Sect. 4, analyzing the use of a single or a parallel arrangement of solar dishes, the adopted size of the TES unit, the performance of the entire solution, and its economic and environmental impact. Finally, conclusions are drawn in Sect. 5.

## 2. Description of the thermal cycle

The proposed cycle depicted in Fig. 1 integrates solar dish collectors (a parallel arrangement can be used to scale up solar thermal power) (a) and a solid state thermal energy storage system (TES) (b), governed by a set of valves controlling the system operation. The cycle is connected to external

energy sources (c), preferably those of renewable origin, which may provide additional energy in the heater (d) to satisfy the constant demand profile ( $\dot{Q}_{ref} \simeq 27$  kW at  $T_{ref} = 1000$  K) of a given industrial activity (e). It is also acceptable if the heat supply eventually exceeds these reference values. Compressed air at about 5 bar (see e.g. [8, 9] for similar air conditions) is used as the Heat Transfer Fluid (HTF). Pressure drop throughout the entire system has not been considered in this work because it will depend on the actual layout of the cycle.

As shown in Fig. 2, air passes through solar dishes and undergoes a temperature increase due to concentrated solar radiation. Subsequently, the heated flowstream enters the TES unit or bypasses it, following a simple decision-making algorithm (see Sect. 3.2) applied at point *O* in Fig. 1 to ensure that the reference conditions for the demand (e) are met with the lowest energy, supported by the external backup (d) if required.

The TES is a solid-state thermal battery consisting of carbon-porous blocks with high thermal conductivity, intended for heat charge or discharge. The material fillers allow for high temperature ( $> 2000$  °C) storage (see a similar solution in [24, 25]). This thermal storage plays a dual purpose in the cycle. On one hand, it facilitates an increase in the temperature of the mass flow passing through the unit when the solid temperature is high enough. On the other hand, the

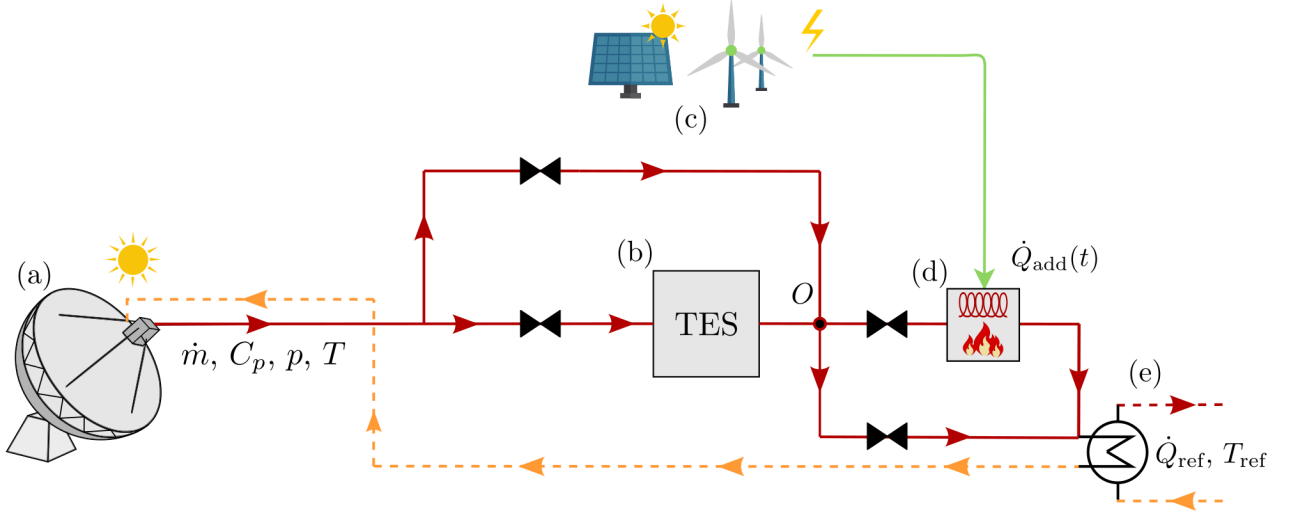


Figure 1: Schematic of the proposed thermal cycle with external energy hybridization (preferably from renewable origin). The thermal elements considered in this work are labeled as: (a) solar dish, (b) thermal energy storage (TES), (c) external energy sources (preferably of renewable origin) and (d) external heater to meet the demand for industrial activity (e) at  $\dot{Q}_{ref} \simeq 27 \text{ kW}$  at  $T_{ref} = 1000$ .

heat accumulated in the TES is transferred back to the airflow when the algorithm requires it. It is important to note that while more sophisticated decision-making strategies could be implemented involving either price or  $\text{CO}_2$  emissions, this study adopts in contrast a simplified logic centered primarily on thermal processes. The evaluation of alternative control methodologies remains a subject for future research.

To carry out a comprehensive analysis, time series from two specific locations in Andalusia (southern Spain), Córdoba and Málaga, which rely on abundant solar resources, were used. The data included direct normal irradiance (DNI) and ambient temperature. In addition to the works of García Ferrero et al. [9] and Zhu et al. [8], Migliari et al. [29] also conducted a similar unsteady anal-

ysis. For conciseness, this study only addresses the case in which TES is initially discharged (i.e., it is uniformly set at the waste or return temperature  $T_w = 500 \text{ K}$ ).

### 3. Description of the numerical models involved in the cycle

#### 3.1. Solar dish model

The thermal model that predicts the performance of the solar dish integrated in the cycle (see Fig. 2) is described below. It is worth mentioning that while this model shares similarities with the approaches by García Ferrero et al. [9] and Zhu et al. [8], some additional features have been incorporated. The following approach will be detailed from the existing zones (1-4) in the receiver:

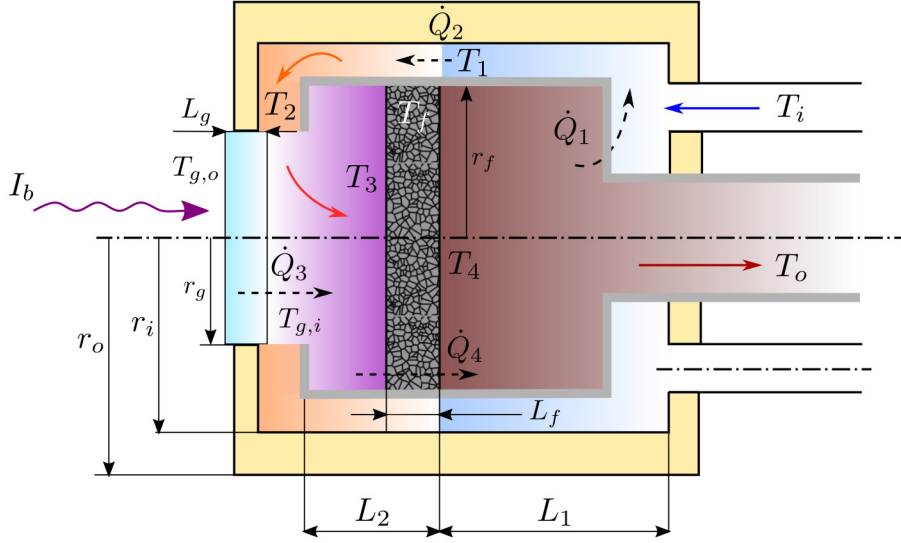


Figure 2: Schematic of the solar dish receiver modeled in this work. The volume is divided into four zones, each representing a different heat transfer process: Zone 1 (blue), Zone 2 (orange), Zone 3 (purple), and Zone 4 (reddish brown). For simplicity, the heat losses are not shown in the figure.

In Zone 1, the heat transfer fluid (air) enters the receiver from the waste/return temperature delivered by the industrial process  $T_i$ . It undergoes a progressive heat exchange with the inner cylinder wall (zone 4 heated by foam) until temperature  $T_1$  is reached. At the same time, the air stream that passes through the foam at temperature  $T_4$  leaves the receiver at the lower temperature  $T_o$ . The energy balance relating heat exchange between zones 1 and 4 reads

$$\dot{Q}_1 = \dot{m} C_p(T_{i,1})(T_1 - T_i) = \dot{m} C_p(T_{4,o})(T_4 - T_o), \quad (1)$$

indicating  $C_p(T_{a,b})$  the  $C_p$  coefficient at the average temperature between  $a$  and  $b$ . Additionally, Zone 1 can be considered as a counterflow heat exchanger (see, e.g. [30]) so that the heat exchange  $\dot{Q}_1$  can be alternatively expressed by us-

ing the (natural) logarithmic mean temperature difference (LMTD), i.e.

$$\dot{Q}_1 = U_1 A_1 \frac{(T_o - T_i) - (T_4 - T_1)}{\log \frac{T_o - T_i}{T_4 - T_1}}, \quad (2)$$

where  $U_1$  is the overall (conduction and convection) heat transfer coefficient per unit area of Zone 1, and  $A_1$  the heat exchange area involved in the process. The heat transfer coefficient  $U_1$  has been calculated as in [9] to account for the convection of  $T_i$  to  $T_1$  and from  $T_4$  to  $T_o$ , and for the conduction through the wall between  $T_i$  and  $T_o$ .

In Zone 2, the temperature increase from  $T_1$  to  $T_2$  undergone by the mass flow can be expressed as a convection process,

$$\dot{Q}_2 = \dot{m} C_p(T_{1,2})(T_2 - T_1). \quad (3)$$

Similarly to Zone 1,  $\dot{Q}_2$  can also be calculated as

the heat transfer in a counter-flow heat exchanger,

$$\dot{Q}_2 = h_w A_2 \frac{(T_w - T_1) - (T_w - T_2)}{\log \frac{T_w - T_1}{T_w - T_2}}, \quad (4)$$

where  $h_w$  is the convective heat transfer coefficient at the inner cylinder wall, while  $A_2$  is the surface area. The wall temperature  $T_w$  is involved in radiative heat exchange as a gray body. According to the approach by Zhu [8], the thermal equilibrium reads as follows,

$$\dot{Q}_2 = \varepsilon_w F_{fw} [\varepsilon_f A_f \sigma (T_f^4 - T_w^4) + \tau_g \rho_f I_b], \quad (5)$$

with  $\varepsilon_w$  the emissivity,  $A_f = \pi r_f^2$  and  $T_f$  the cross-sectional area and the temperature of the foam,  $F_{fw}$  the view factor between the foam and the inner cylinder wall,  $\tau_g$  the glass window transmissivity,  $\rho_f$  the reflectivity of the foam,  $I_b$  the solar radiation power, and  $\sigma$  the Stephan-Boltzmann constant.

Later, during heat transfer from  $T_2$  to  $T_3$ , the air flow exchanges heat with the inner surface of the glass in Zone 3 [8]. The process can be expressed as the convective heat exchange given by

$$\begin{aligned} \dot{Q}_3 &= \dot{m} C_p (T_{2,3}) (T_3 - T_2) \\ &= A_g h_{g,i} \frac{(T_{g,i} - T_2) - (T_{g,i} - T_3)}{\log \frac{T_{g,i} - T_2}{T_{g,i} - T_3}}. \end{aligned} \quad (6)$$

However, the temperature increase experienced by the glass window due to incident solar radiation is analyzed separately for the inner and outer surfaces (see Appendix A.3 for further information). For the outer surface of the glass window, heat flow  $\dot{q}_{g,o}$  can be defined from the next balance

equation

$$\dot{q}_{g,o} A_g = h_{g,o} A_g (T_a - T_{g,o}) + \varepsilon'_g A_g \sigma (T_a^4 - T_{g,o}^4), \quad (7)$$

and for the inner border  $\dot{q}_{g,i}$  can be obtained from

$$\begin{aligned} \dot{Q}_3 &= \dot{q}_{g,i} A_g + \alpha'_g F_{fg} \varepsilon_f A_f \sigma (T_f^4 - T_{g,i}^4) \\ &\quad + \alpha'_g F_{wg} \varepsilon_w A_w \sigma (T_w^4 - T_{g,i}^4), \end{aligned} \quad (8)$$

with  $T_{g,o}$  and  $T_{g,i}$ , the outer and inner glass temperatures,  $T_a$  the ambient temperature,  $A_g = \pi r_g^2$  the cross-sectional (effective) area of the glass surface.

The outer border balance in Eq. (7) relates the convective and radiative heat exchanges from the glass window with the surroundings with the diffusive heat flux at the glass outer border  $\dot{q}_{g,o}$ . In contrast, Eq. (8) relates the inner diffusive flux  $\dot{q}_{g,i}$  with the heat transfer to the fluid by convection  $\dot{Q}_3$ , end the radiative exchange with the foam at  $T_f$  and the wall at  $T_w$ .

In Zone 4, the air has passed through the nickel foam, absorbing the necessary heat to increase the temperature to  $T_4$ . The heat exchange across the foam can be considered convective, i.e.

$$\dot{Q}_4 = \dot{m} C_p (T_{3,4}) (T_4 - T_3) = h_{sf} A_{sf} (T_f - T_{34}), \quad (9)$$

where  $T_{34}$  is the average temperature between zones 3 and 4. Since the metal foam is treated as a porous medium,  $h_{sf}$  and  $A_{sf}$  represent the specific convective heat transfer coefficient and the specific surface area of the structure respectively.

The latter is given by Zhu et al. [8]:

$$A_{sf} = \frac{3\pi d_f}{(0.59 d_p)^2} \left[ 1 - \exp \left( -\frac{1 - \phi}{0.04} \right) \right], \quad (10)$$

with  $d_f$  the thickness of the foam. The ratio between the porous diameter  $d_p$  and the foam thickness can be expressed as

$$d_f/d_p = 1.18 \sqrt{\frac{1-\phi}{3\pi}} \frac{1}{1 - \exp[-(1-\phi)/0.04]}. \quad (11)$$

The specific heat transfer coefficient  $h_{sf}$  is typically taken from the work of Žukauskas [31], as previously done by e.g. Zhu et al. [8] and Zhao et al. [32].

On the other hand, thermal losses have been computed as in Zhu et al. [8] as follows,

$$\dot{Q}_{g,emission} = \varepsilon'_g A_g \sigma (T_g^4 - T_a^4), \quad (12)$$

$$\dot{Q}_{g,reflectance} = \rho_g I_b, \quad (13)$$

$$\dot{Q}_{f,emission} = \tau'_g F_{fg} \varepsilon_f A_f \sigma (T_f^4 - T_a^4), \quad (14)$$

$$\dot{Q}_{f,reflectance} = \tau'_g F_{fg} \rho_f I_b, \quad (15)$$

$$\dot{Q}_{w,emission} = \tau'_g F_{wg} \varepsilon_w A_w \sigma (T_w^4 - T_a^4), \quad (16)$$

$$\dot{Q}_{convection} = A_g h_{go} (T_g - T_a), \quad (17)$$

which leads to a heat power total loss

$$\begin{aligned} \dot{Q}_{loss} = & \dot{Q}_{g,emission} + \dot{Q}_{g,reflectance} \\ & + \dot{Q}_{f,emission} + \dot{Q}_{f,reflectance} \\ & + \dot{Q}_{w,emission} + \dot{Q}_{convection}. \end{aligned} \quad (18)$$

The overall efficiency of the dish can be expressed as the usual ratio between the energy input and the output, i.e.

$$\eta = 1 - Q_{loss}/I_b, \quad (19)$$

where  $I_b$  is the solar radiation power.

The nonlinear algebraic system Eqs. (1) to (9) has been implemented in Python and solved using

the root function with the Levenberg-Marquardt method [33] (see the SciPy optimization toolbox [34]). Unless otherwise specified, the heat transfer coefficients are calculated following the work of García Ferrero et al. [9]. As remarked by them, there is a minimum DNI quantity ensuring the convergence of the system of equations. In the current study, the reference  $I_b^0 = 7$  kW has been selected as the threshold value to start the solar dish simulations (notice the mismatch in Fig. 4 comparing  $I_b$  with the rest of the magnitudes). Finally, the validation of the solar dish model is shown in Appendix A.

### 3.2. TES model

The TES unit has been modeled following the work by Schumann [35], which accounts for the one-dimensional convective heat transfer of a fluid at a temperature  $T$  that flows through a solid porous medium at a temperature  $T_s$  (indistinctly if it is colder or hotter than that of the fluid). Because thermal diffusive effects and external heat sources are considered here, the governing equations become

$$\begin{aligned} \epsilon \left( \frac{\partial T}{\partial t} + u_0 \frac{\partial T}{\partial x} \right) = & \epsilon \alpha \frac{\partial^2 T}{\partial x^2} \\ & - \frac{\lambda_v}{\rho(T) C_p(T)} (T - T_s), \end{aligned} \quad (20)$$

$$\begin{aligned} (1 - \epsilon) \frac{\partial T_s}{\partial t} = & (1 - \epsilon) \alpha_s \frac{\partial^2 T_s}{\partial x^2} \\ & + \frac{\lambda_v}{\rho_s(T) C_{ps}(T)} (T - T_s), \end{aligned} \quad (21)$$



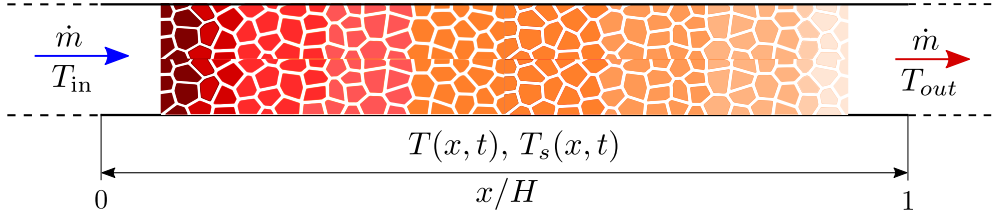


Figure 3: Schematic of the thermal storage system. The porosity of TES in the figure is depicted arbitrarily.

which have to be solved with the appropriate boundary conditions

$$T = T_{\text{in}}, \quad \frac{\partial T_s}{\partial x} = 0, \quad \text{at } x = 0, \quad (22)$$

$$\frac{\partial T}{\partial t} = \frac{\partial T_s}{\partial x} = 0, \quad \text{at } x = L, \quad (23)$$

being  $\epsilon$  the void fraction or porosity,  $u_0 = u/\epsilon$  the interstitial velocity,  $\alpha = k/(\rho C_p)$  and  $\alpha_s = k_s/(\rho_s C_{ps})$  the respective thermal diffusivity for the fluid and the solid phase,  $k$  and  $k_s$  the conduction coefficients,  $C_p$  and  $C_{ps}$  the specific heats at constant pressure, and  $\lambda_v$  the heat transfer coefficient. The initial conditions consider that both fluid and solid are in thermal equilibrium, i.e.

$$T = T_s = T_0, \quad \text{at } t = 0. \quad (24)$$

It is worth mentioning that although some authors [15, 36] introduced additional terms for the improvement of Eqs. (20) and (21) (e.g. the influence of the external wall, thermal losses, or the intra-particle diffusion), it has been shown that the results are practically unchanged compared to those obtained using Schumann's original model [35].

Equations (20) to (24) have been implemented numerically by adopting a finite difference scheme. The diffusive terms are discretized

following a second-order central differencing [37], while the convective term has been upwinded. The temporal discretization follows an implicit Euler method. The PDE system has been implemented in Python using differentiating matrices to exploit the NumPy[38] capabilities. Exclusively one (temporal) loop exists in the code. Appendix A.3 shows the validation of the TES numerical model.

Finally, for the actual TES used in the proposed thermal cycle, the thermophysical properties of the carbon blocks are described in Table 1.

### 3.3. Combined dish-TES performance model

Because the waste heat temperature has been considered constant, the temperature of the air exiting a solar dish will depend exclusively on the dish size, the thermophysical properties of the receiver, the mass flow rate (this will be affected by the number of dishes in parallel connection) and the DNI. Therefore, the solar dish performance remains disconnected from the rest of the elements of the cycle. However, the role of the TES may adopt different actuation strategies switching between charge, discharge, or bypass modes, depending on the following simple decision-making

Table 1: Thermophysical properties of the carbon-block TES material (temperatures in K where needed). Data taken from Butland and Maddison [39].

$\rho_G$	kg m <sup>-3</sup>	1800
$Cp_G$	J kg <sup>-1</sup> m <sup>-1</sup>	4184 (0.54 + 9.11 × 10 <sup>-6</sup> $T$ - 90.27 $T^{-1}$ + 1.593 × 10 <sup>7</sup> $T^{-3}$ - 1.4379 × 10 <sup>9</sup> $T^{-4}$ )
$k_G$	W m <sup>-1</sup> K <sup>-1</sup>	120

algorithm:

1.  $T_{in} \geq T_{ref}$  and  $T_{TES}^o \geq T_{ref}$ : Charge,
2.  $T_{in} \geq T_{ref}$  and  $T_{TES}^o < T_{ref}$ : Bypass,
3.  $T_{in} < T_{ref}$  and  $T_{TES}^o \geq T_{ref}$ : Bypass,
4.  $T_{in} < T_{ref}$  and  $T_{in} < T_{TES}^o$  and  $T_{TES}^o < T_{ref}$   
and  $T_{TES}^o < 510$  K: Bypass,
5.  $T_{in} < T_{ref}$  and  $T_{in} < T_{TES}^o$  and  $T_{TES}^o < T_{ref}$   
and  $T_{TES}^o \geq 510$ : Discharge.

In charge mode, a high air temperature is used to increase the temperature of the solid fillers within the TES. When the air temperature drops, the process is reversed to energize the airstream through the TES discharge. Otherwise, the temperature level of the TES is considered to have marginal benefits (or drawbacks), and the bypass mode is activated. After each of these actions, a certain additional power  $\dot{Q}_{add}(t)$  is applied to the mass flow to reach and maintain the reference conditions. It should be noted that this is a reasonable and extremely simple strategy aimed at reducing the additional energy  $Q_{add}$  to overcome the thermal requirements of industrial activity. Of course, it is not the best. More elaborated algorithms might involve the instantaneous price

of the energy and the CO<sub>2</sub> emissions.

The combination of the thermal elements described in Sect. 3.1 and in Sect. 3.2 has been implemented by directly connecting the outlet temperature of the solar dishes to the corresponding element of the cycle, depending on the aforementioned operating modes. Thus, the TES boundary condition Eq. (22) becomes time dependent, and in consequence it may switch between Dirichlet (in charge or discharge modes),

$$T(t) = T_{in}(t) \equiv T_{os}(t), \quad \frac{\partial T_s}{\partial x} = 0, \quad \text{in } x = 0. \quad (25)$$

and Neumann (or adiabatic) type (when the bypass mode is enabled),

$$\frac{\partial T}{\partial x} = \frac{\partial T_s}{\partial x} = 0, \quad \text{in } x = 0. \quad (26)$$

The outlet boundary conditions remain unchanged from those of the original model [Eq. (22) and Eq. (23)], independently of the operation mode.

Although it might be argued that Eqs. (1) to (9) is a steady-state formulation, a quasi-steady approach has been considered in this work because the time response of the solar dish is slow (typically hours, as shown in Fig. 4) compared to the

convective scale  $L/u_0$  corresponding to the TES, which is of order of seconds.

For illustration's sake, Fig. 4 shows the output temperature of the solar dish of 44 m<sup>2</sup> used in [8, 9] energizing the same mass flow ratio as that used by Pacheco et al. [40] ( $\dot{m} = 0.043$  kg/s). The waste heat temperature has been fixed to the constant value  $T_w = 500$  K, which is similar to that used by [9] (528.66 K/493.88 K in June 22<sup>nd</sup>/Dec. 22<sup>nd</sup>), so it will be assumed that the mass flow returns to the dishes at that value.

## 4. Results and discussion

### 4.1. Solar dish performance for $N = 1, 2$ and 4 dishes in parallel connection

The solar contribution for  $N = 1, 2$  and 4 dishes in parallel connection (this choice will be justified in Sect. 3.2) is firstly analyzed in Fig. 4 across the days March 22<sup>nd</sup> (a), June 22<sup>nd</sup> (b) and December 22<sup>nd</sup> (c), at the selected locations of southern Spain (Córdoba and Málaga). The number of dishes in parallel (if any) is taken into account in the numerical model through the mass flow rate so that  $\dot{m} = \dot{m}_0/N$ , with  $\dot{m}_0 = 0.043$  kg/s (as previously discussed). The inlet temperature is that of the waste heat, that is  $T_{in} = T_w$ .

When a single dish is used ( $N = 1$ ), the highest outlet temperatures reach about 500 °C, 750 °C and 250 °C on the respective selected days of study (a)–(c) and (d)–(f). The maximum efficiency [see Eq. (19)] of the solar dish considering

the inlet temperature as  $T_w$ , is  $\eta_{max} \simeq 72\%$ , which is found on March 22<sup>nd</sup> and June 22<sup>nd</sup>. However, on December 22<sup>nd</sup> the radiation quantity impinging the dish decays dramatically, leading to a lower efficiency 10%, i.e.  $\eta \simeq 62\%$ . It can be observed that the influence of location is practically indistinguishable in terms of the DNI (note the temporal evolution of  $I_b$ , and only a slightly thinner profile can be identified when comparing (c) vs. (f). In contrast, the ambient temperatures present larger differences due to the coastal influence in Málaga, but eventually this results in very small differences in  $T_o$ .

For two dishes in parallel connection ( $N = 2$ ), Fig. 4 shows a significant increase in the outlet temperature, as expected. The maximum temperature at which the airstream exits each of the dishes is now around 750 °C [(a), (d)], 900 °C [(b), (e)] and 500 °C [(c), (f)], i.e. a 50%, a 20% and a 100% compared to the case with  $N = 1$ . In this configuration, the resultant dish efficiency remains practically invariable with respect to the former case. This is explained by the fact that thermal losses increase with increasing temperature, for the same ambient temperature, as can be deduced from Eq. (19).

If the number of dishes in parallel connection is increased to four ( $N = 4$ ), the efficiency of the dish experiences a sudden drop at noon on March 22<sup>nd</sup> and June 22<sup>nd</sup>. These hours coincide with higher levels of  $I_b$ , leading to peak outlet tem-

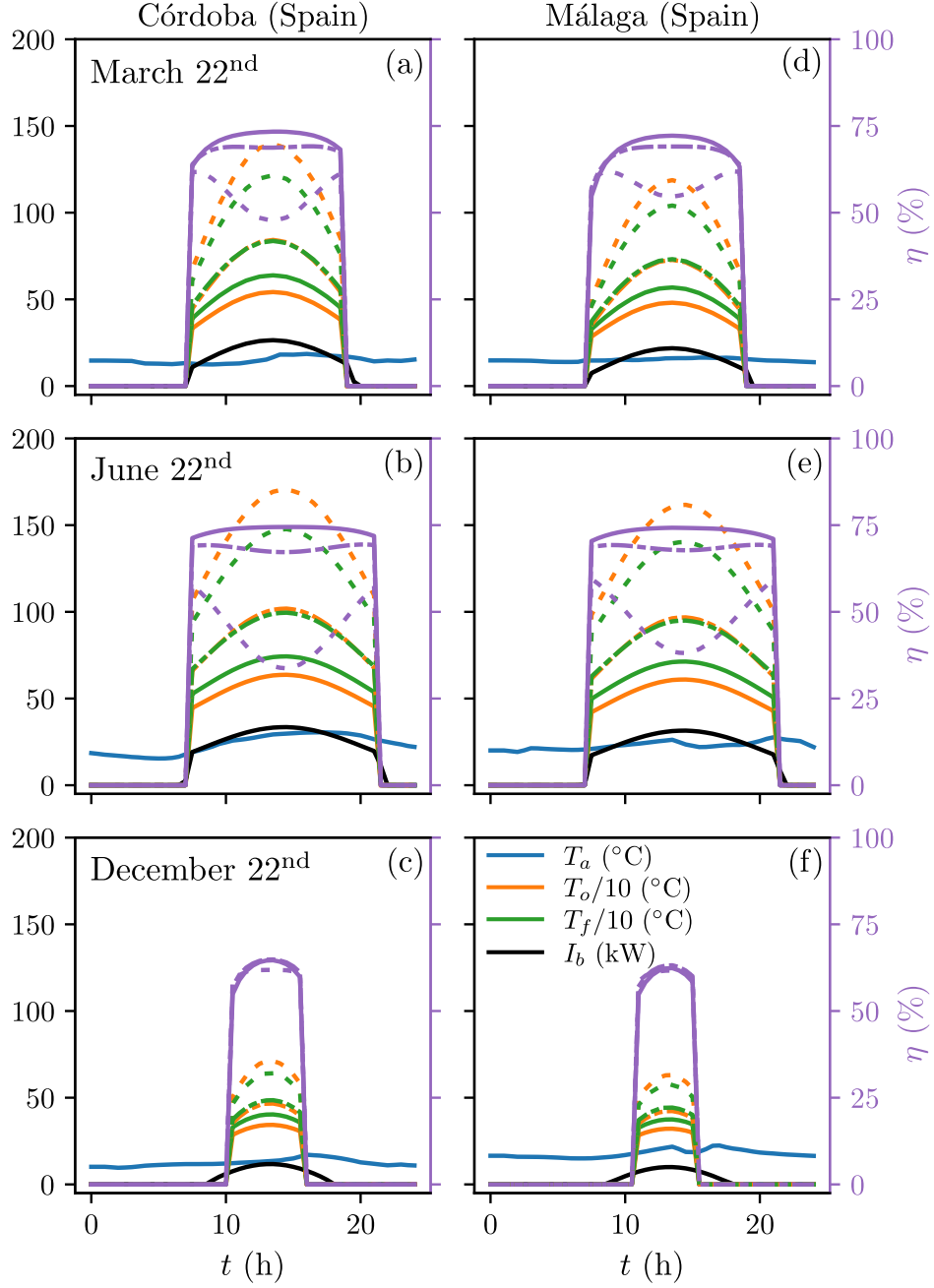


Figure 4: Temporal evolution of the (scaled) ambient  $T_a$ , output  $T_o$  and foam  $T_f$  temperatures, solar irradiance  $I_b$ , and dish performance  $\eta$  for each of the indicated days in Córdoba (a)–(c) and in Málaga (d)–(f). Solid lines: one solar dish ( $N = 1$ ), dashed: two solar dishes in parallel connection ( $N = 2$ ), dashed-point: four solar dishes in parallel connection ( $N = 4$ ).

peratures about 1400 °C [(a), (d)], 1600 °C [(b), (e)] and 600 °C [(c), (f)]. As a result, the thermal losses on March 22<sup>nd</sup> and June 22<sup>nd</sup> are high enough to decrease the value of  $\eta_{max}$ , even below

the efficiency observed during the early hours of the day.

#### 4.2. TES sizing procedure

A single TES unit either receives the mass flow exiting the solar dishes at the corresponding outlet temperature (in charge or discharge modes) or it only contains and evolves the heat transfer internally (bypass mode). Although the surface of the CSP has been fixed at  $44 \text{ m}^2$  (as used by [8, 9]), the TES size needs to be determined. Buckingham's  $\pi$  theorem is an effective method to establish a functional dependence among a set of reduced dimensionless parameters [41, 42]. Because one of the main interests in this work is to determine the most convenient size of the TES to reduce the additional energy  $Q_{\text{add}}$  necessary to reach the reference, the following dependence can be established,

$$Q_{\text{add}} = f(L, D, \dot{m}, \dot{m}_0, \rho_0), \quad (27)$$

where  $L$  is the TES length,  $D$  is the diameter,  $\dot{m}$  is the mass flow rate passing through each of the dishes,  $\dot{m}_0 = 0.043 \text{ kg/s}$  is the total mass flow rate considered in this work, and  $\rho_0$  is the air density in standard conditions. With these variables, the basic magnitudes of *length*, *mass* and *time* are covered, and three independent dimensionless groups can be built,

$$\tilde{Q}_{\text{add}} \equiv Q_{\text{add}} \frac{\rho_0 D}{\dot{m}_0^2} = f(L/D, \dot{m}_0/\dot{m} \equiv N), \quad (28)$$

namely the dimensionless energy  $\tilde{Q}_{\text{add}}$ , the aspect ratio  $L/D$  and the number of solar dishes in parallel connection  $N$ . However, because  $\dot{m}_0^2$  is very

small, it is convenient to reformulate Eq. (28) as

$$\begin{aligned} \tilde{Q}_{\text{add}} \equiv Q_{\text{add}}/Q_0 &\equiv \frac{Q_{\text{add}}}{\dot{m} C_p(\bar{T})(T_{\text{ref}} - T_w) t_{\text{day}}} \\ &= f(L/D, N), \end{aligned} \quad (29)$$

with

$$Q_0 \equiv \dot{m} C_p(\bar{T})(T_{\text{ref}} - T_w) t_{\text{day}} \quad (30)$$

the amount of energy required to elevate the waste temperature  $T_w$  to that of reference  $T_{\text{ref}}$  demanded by the industrial activity ( $\dot{Q}_0 \simeq 27 \text{ kW}$  and  $Q_0 \simeq 650 \text{ kWh}$ ).

Figure 5 displays the relationship Eq. (29) in terms of the energy reduction  $\mathcal{R}$  with respect to  $Q_0$ ,

$$\mathcal{R} \equiv 1 - \frac{\bar{Q}_{\text{add}}}{Q_0}, \quad (31)$$

where  $\bar{Q}_{\text{add}}$  stands for the yearly-averaged added energy defined as

$$\bar{Q}_{\text{add}} = \frac{1}{t_y} \int_0^{t_y} Q_{\text{add}}(t) dt, \quad (32)$$

with  $t_y$  the total yearly time in the corresponding units. Because the days in the study represent two solstices (22<sup>nd</sup> June and 22<sup>nd</sup> December) and one equinox (22<sup>nd</sup> March), Eq. (32) can be approximated by

$$\bar{Q}_{\text{add}} \simeq \frac{1}{4} \left( 2 Q_{\text{add}}^{22^{\text{nd}} \text{ March}} + Q_{\text{add}}^{22^{\text{nd}} \text{ June}} + Q_{\text{add}}^{22^{\text{nd}} \text{ Dec}} \right), \quad (33)$$

assuming that the year 2022 is fully represented by these four dates, and that the fall equinox is similar to that of spring.

The calculation of each term  $Q_{\text{add}}^i$  (with  $i = 22^{\text{nd}} \text{ March}, 22^{\text{nd}} \text{ June}, \text{ or } 22^{\text{nd}} \text{ December}$ ) in

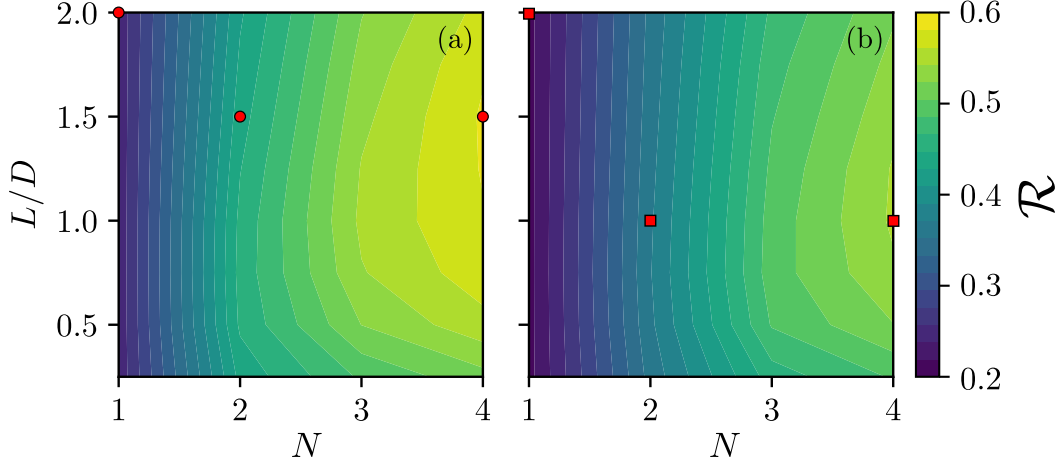


Figure 5: Summary of the energy reduction  $\mathcal{R}$  given by Eq. (31) with respect to the aspect ratio  $L/D$  and to the number of dishes in parallel  $N$ .

Eq. (33) has been conducted by integrating numerically the system of equations governing the entire cycle operation (see Sect. 3),

$$Q_{\text{add}}^i = \int_{0 \text{ h}}^{24 \text{ h}} \dot{Q}_{\text{add}}^i(t) dt, \quad (34)$$

where  $\dot{Q}_{\text{add}}^i(t)$  is the heat power necessary to overcome the industrial demand instantaneously. The numerical code has been run for the ranges  $0.25 \leq L/D \leq 2.00$  and  $1 \leq N \leq 4$ , at the two locations in the study. Fixed  $D = 1$  m as the diameter of the TES, the sensitivity analysis in Fig. 5 illustrates that the maximum energy savings in  $Q_{\text{add}}$  occur for  $N = 4$  dishes in parallel and for the aspect ratios  $L/D = 1.5$  in Córdoba and  $L/D = 1.0$  in Málaga.

Unlike Van Lew et al. [43], where the sizing of a molten salt tank (with similar charge/discharge operation modes) was calculated for steady state inlet conditions, the current approach offers a more accurate tool capable of handling time-

varying inlet temperatures. Figure 6 and Fig. 7 in Sect. 4.3 depict the time evolution of some magnitudes of interest for the selected points marked in Fig. 5 at the two distinct locations, one of them representing, of course, the most suitable TES size according to this approach.

#### 4.3. Combined dish-TES operation

Figures 6 and 7 show the numerical results of the whole cycle operation, according to the models in Sect. 3. For the various combinations of  $L/D$  and  $N$  selected in Fig. 5, these graphs show the daily evolution of the outlet temperatures from the solar dish and from the TES, as well as the additional power and added energy, for the selected days of the year. Note that the charge/discharge and bypass modes of the TES unit are identified in Figs. 6 and 7, providing useful information for cycle analysis.

First, as can be for the configurations consider-

ing only one dish, Figs. 6 and 7(a), (d), and (g), show that the solar resource never exceeds the reference temperature during that day, indicating that no charge or discharge processes occur at any of the chosen locations, and the TES is always bypassed. As a result, the energy captured by the solar dish is the only input received by the cycle, which must be compensated for the added external power (see the power curve mirroring that of the solar dish outlet temperature  $T_{SD}$ ). In the best cases (on 22 June<sup>nd</sup>), this leads to an energy consumption of 434 and 451 kWh in Córdoba and Málaga, respectively, which represents about 30–33% energy savings with respect to cycle performance without any support. On December 22<sup>nd</sup>, the solar contribution is much scarce, and the energy savings decay to 3.8–2.6%.

Alternatively, if two solar dishes are used in parallel connection, the dish outlet temperatures increase considerably, and some of the cases in Figs. 6 and 7(b), (e) and (h) promote the TES operation. For example, regarding the results on March 22<sup>nd</sup> in Córdoba [see Fig. 6(b)], it can be observed that there is a time window around noon where  $T_{SD}$  becomes higher than  $T_{ref}$ , and consequently, the TES charge is activated. Later, once  $T_{SD}$  decays below  $T_{ref}$ , the bypass mode is activated until discharge begins, when  $T_{SD}$  further decreases below the TES temperature in bypass mode ( $T_{TES}^{bp}$ ). The energy savings in this case are  $\simeq 45\%$ , which is substantially greater than those

obtained with  $N = 1$ . It is worth mentioning that the TES charge/discharge modes are not reached in Málaga [see Fig. 7(b)] resulting in energy savings of approximately a 30%, which are comparable to those obtained with  $N = 1$  on June 22<sup>nd</sup> [see Figs. 6 and 7(d)]. On June 22<sup>nd</sup>, the contribution of the dish raises the air temperature above  $T_{ref}$  during most of the solar hours both in Córdoba and Málaga [see Figs. 6 and 7(d)]. This fact enlarges the charge period from approximately 10 to 20 h, and minimizes the bypass actuation, which is of course beneficial (note that bypass mode implies  $\dot{Q}_{add} > 0$ ). It can be observed that external power is added to the system during the first ten hours of the day, and a zero-energy window results for approximately the following 10 hours. Energy savings under these circumstances are greater than 60%, i.e. twice the savings achieved in its counterpart with  $N = 1$  in Figs. 6 and 7(d). In winter [Figs. 6 and 7(d)], the solar power captured by the dish is not enough to overcome the reference temperature, and additional power becomes necessary. The savings in this case are slightly higher than those in Figs. 6 and 7(g), but in any case they are below 8%.

Finally, when four dishes are connected in parallel the temperature of the air exiting the solar dish is further increased with respect to the previous configurations, reaching considerably peak values of about 1400, 1700, and 700 °C in both locations. On March 22<sup>nd</sup> and on June 22<sup>nd</sup>, it can

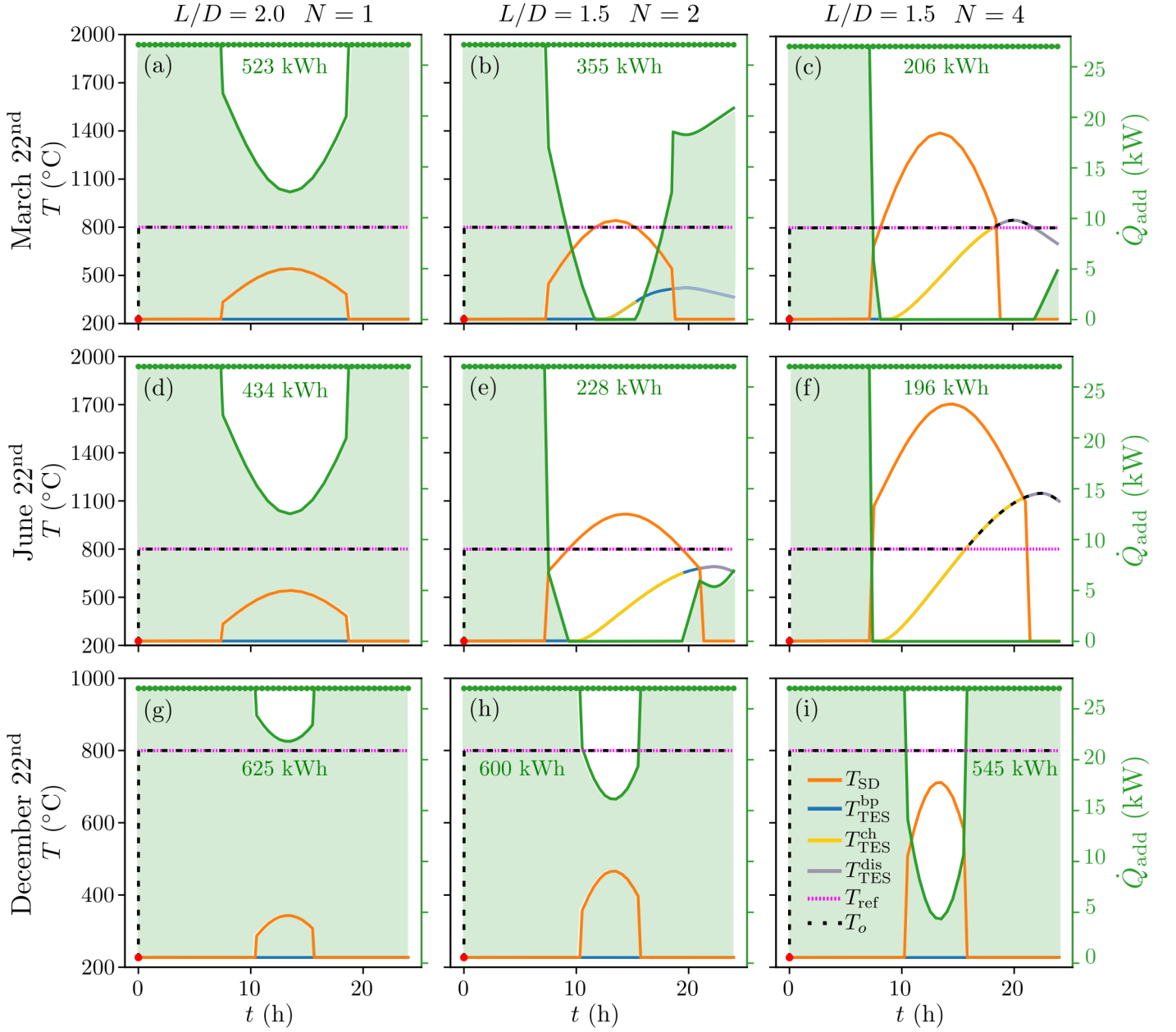


Figure 6: Time evolution of the solar-dish outlet temperature  $T_{SD}$  (orange), and of the air temperatures in the TES in bypass mode  $T_{TES}^{bp}$  (blue), in charging mode  $T_{TES}^{ch}$  (yellow), and in discharge mode  $T_{TES}^{dis}$  (grey). The reference temperature  $T_{ref}$  and the produced temperature are depicted by dashed lines in pink and black, respectively. The right-hand side scale accounts for the additional heat power  $\dot{Q}_{add}$  to reach the industrial demand of 27 kW (bullets line in green). The shaded green area represents the energy consumed during the day given by Eq. (34). The total amount of energy is superimposed (in green). All these results refer to March 22<sup>nd</sup>, June 22<sup>nd</sup> and December 22<sup>nd</sup> in Córdoba, for the configurations indicated on the top.

be seen in Figs. 6 and 7(c) and (f) that  $T_{SD} > T_{ref}$  mode of the TES during that time window, and for practically all solar hours, enabling the charge the discharge from the sunset until the end of the



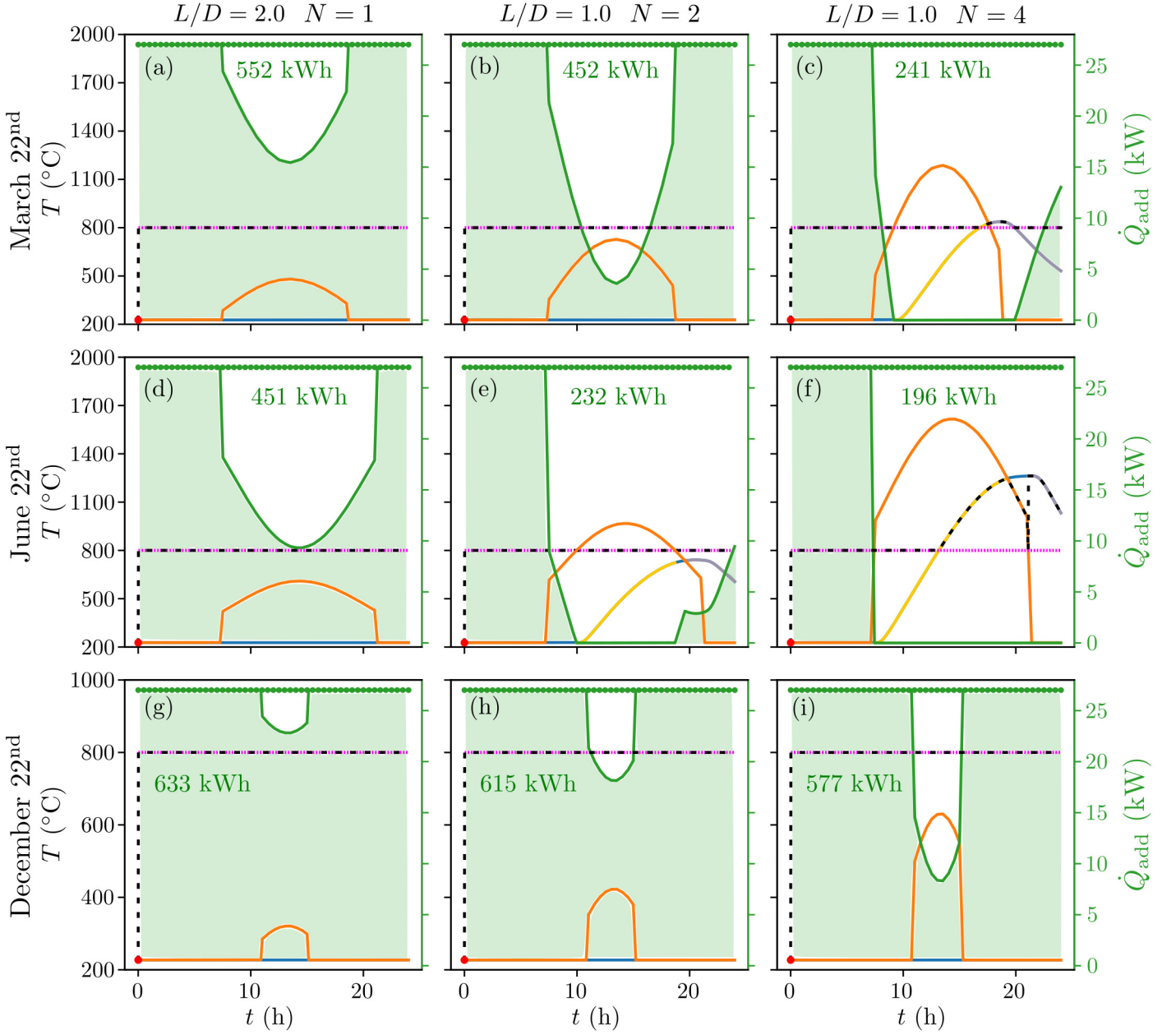


Figure 7: Same as in Fig. 6 but for Málaga.

day. The bypass mode is barely active (only for a short period in Fig. 7(f)). This configuration only requires extra energy during the first third of the day and in the last 2–4 hours, depending on the location [see Fig. 6(c) vs. Fig. 7(c)]. The respective energy reduction on March 22<sup>nd</sup> and on June 22<sup>nd</sup> rises up to a 63–68% and a 70%. The

energy savings in winter are small, but somewhat larger than with the  $N = 2$  configuration (16% in Córdoba and 11% in Málaga).

In summary, one can note that the larger the number of dishes in parallel connection, the higher the air temperature, and therefore the greater the energy amount that can be stored in the TES

unit. Figure 5 illustrates that the TES size needs to be determined analyzing the energy requirements of the cycle. In this work, an energy-based decision-making algorithm has been implemented for simplicity, and the TES size has been adopted accordingly. However, one can see that the energy contained in the thermal battery is not fully discharged at the end of the day, which would set the air temperature at a higher level for the next day, and in practice would indicate that the actual TES size might be smaller. Because the ultimate aim for the real implementation of this proof-of-concept is to estimate the ROI, a more accurate TES sizing will be proposed for future studies, conducting numerical simulations either during more days or analyzing the sensitivity of the initial temperature in the TES.

#### 4.4. *Economical savings and environmental impact*

In addition to the former results in terms of thermal energy and power, it is also convenient to quantify the economical aspects and the equivalent CO<sub>2</sub>-emissions (the latter also involving economical benefits but not considered here) in operating conditions. The electric market will be considered here because historical data on the evolution of Spanish grid pricing are freely available from Red Eléctrica Española [44]. Different energy sources might be considered in future studies.

At first glance, one can observe in Fig. 8(a)

or (b) that while the theoretical energy price on March 22<sup>nd</sup> is comparable to that on June 22<sup>nd</sup>, it was much lower on December 22<sup>nd</sup>, probably due to the wind energy generation. With these rates, the accumulated theoretical prices resulted in about 240, 210 and 75 EUR at the end of the respective days. If one solar dish is introduced, the contribution is clearly observed during the central hours of the day, e.g. through a decreasing curve in (a) and (c), or through a smaller-slope period in (b) and (d). The maximum reduction in the price per hour is reached on June 22<sup>nd</sup> and it is about four times with respect to the instantaneous energy price. However, at the end of the day, the total cost is comparable to that on March 22<sup>nd</sup>, i.e. around 160 EUR. The winter day is by far cheaper than the other two, but this is exclusively due to the fact that the electricity pricing on December 22<sup>nd</sup> was rather low compared to the other days of the study. Energetically, winter is the season receiving fewer amount of solar irradiance.

If the cycle is implemented with four dishes in parallel, in Fig. 8 some free energy periods appear. For example, the operating price in (a) and (c) drops to zero from 9 h until the end of the day on 22 June<sup>nd</sup>, and practically the same happens on 22 March<sup>nd</sup>. This can be observed as a plateau in the charts (b) and (d), where the accumulated price no longer increases. In these cases, the total price at the end of the day is about 50 and 75 EUR.

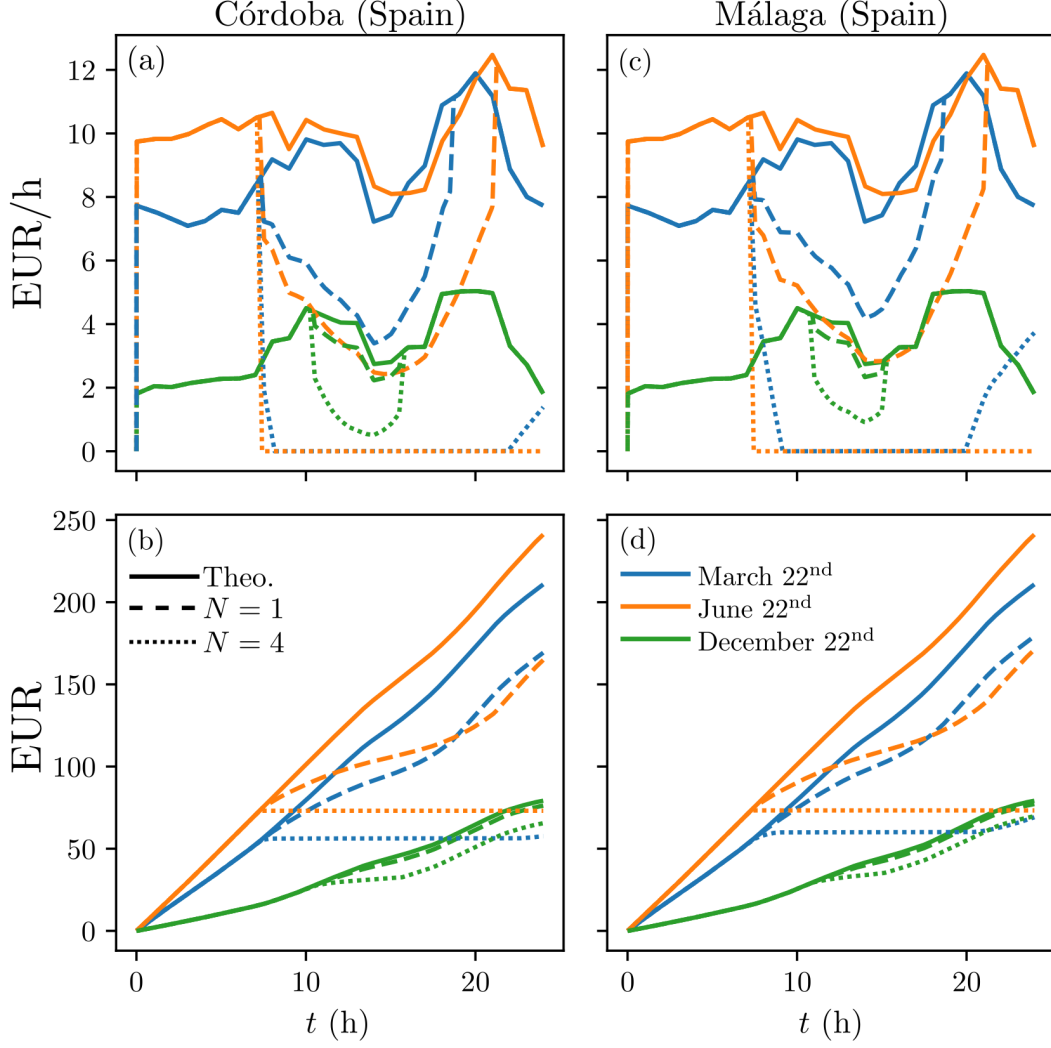


Figure 8: Temporal evolution of the respective cost per hour and of the (accumulated) cost in Córdoba (a), (b) and in Málaga (c), (d), for the days in the study. Solid line: theoretical cost satisfying the industrial demand without dish or TES, dashed: cost with  $N = 1$  solar dish and  $L/D = 2$ , dotted: cost with  $N = 4$  dishes in parallel and  $L/D = 1.5$  (for Córdoba) and  $L/D = 1.0$  (for Málaga).

On December 22<sup>nd</sup>, the free energy condition is not met and the final price results in  $\simeq 62$  EUR.

Alternatively, Fig. 9 compares (a) the additional energy and (b) its (electric) cost for the different CSP-TES configurations in Córdoba and Málaga, for each day of the study. It is clearly visible that  $Q_{\text{add}}$  decreases monotonically with the number of dishes in parallel connection, which ba-

sically is an illustrative summary of Fig. 6 and Fig. 7. Obviously, the days with a smaller input of  $Q_{\text{add}}$  are those receiving a considerable  $I_b$  quantity, i.e. March 22<sup>nd</sup> and June 22<sup>nd</sup> at both locations. Although it had been discussed that the environmental conditions of Córdoba and Málaga are quite similar, there is a noticeable difference of  $\simeq 100$  kWh in Fig. 9(a) on March 22<sup>nd</sup>. How-

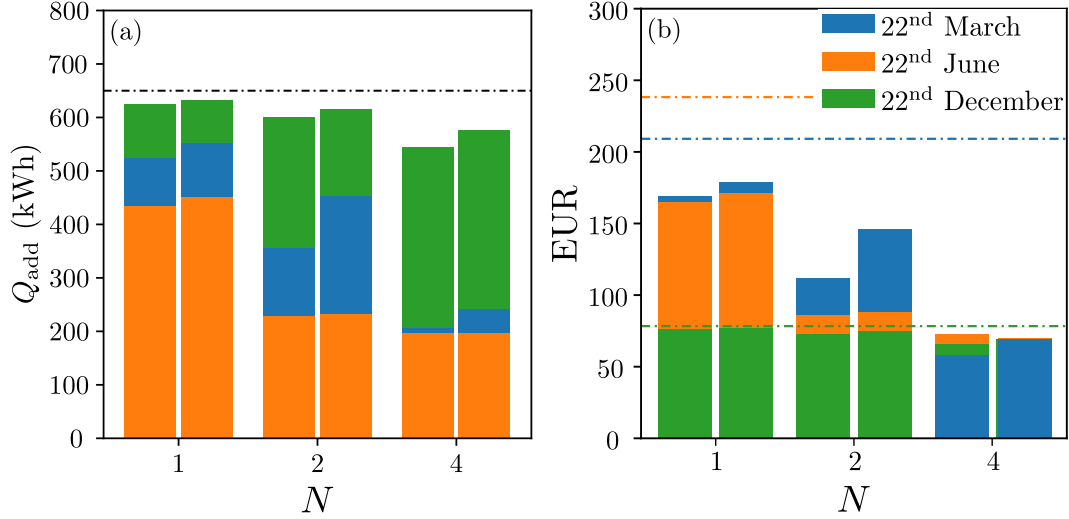


Figure 9: Comparison of the overall energy (a) and cost (b) of the cycle operation for the different configurations marked in Eq. (31), for each of the days in the study. Left columns of each pair indicate Córdoba, and right columns Málaga. Black dashed-dotted line is the required theoretical energy, and colored dashed-dotted lines indicates the accumulated cost per each of the days in the legend.

ever, in economic terms, it does not follow the same trend because the amount of renewable energy production (see Sect. 4.4 in terms of  $\text{CO}_2$ ) on December 22<sup>nd</sup> decreased the prices of the electric market substantially, as can be observed in Fig. 9(b). This situation leads to the case where  $N = 4$ , and  $Q_{add}$  is so small (due to the large received energy) that it surpasses (or compensates) the excessively cheap price of energy on December 22<sup>nd</sup>. More particularly, the cost in Córdoba follows the  $Q_{add}$  trend in (a), i.e. the larger the additional energy, the more expensive the cycle operation on that day. In Málaga, it barely reaches an equilibrium point, meaning that regardless of the day of analysis, the operating cost will remain the same.

In terms of  $\text{CO}_2$  emissions, Sect. 4.4 summarizes the equivalent quantity in kilograms, com-

paring the result obtained under different configurations ( $N, L/D$ ) for each of the days and locations in this study. For reference's sake, the total amount of emissions of the cycle operating only consuming electrical energy from the Spanish grid (theoretical case) are 71, 105 and 39  $\text{CO}_2$  eq. kg on March 22<sup>nd</sup>, June 22<sup>nd</sup> and on December 22<sup>nd</sup>, respectively. A general look at Sect. 4.4 shows that the amount of  $\text{CO}_2$  emissions is consistent with the price of energy because lower emissions mean more renewable generation and consequently a more competitive energy pricing. With  $N = 1$ , the percentage of reduction with respect to the theoretical case represents about 15%, 26%, and 2%, respectively. If two dishes are connected in parallel, the decarbonization of the industrial activity may reach 37%, 57%, and 5%. More friendly with the environment is the config-

Table 2: CO2 equivalent kilograms emitted at each location for each day of the study. For  $N = 1$ ,  $N = 2$  and  $N = 4$ , CO2 eq. kg in Córdoba / CO2 eq. kg in Málaga.

	March 22 <sup>nd</sup>	June 22 <sup>nd</sup>	December 22 <sup>nd</sup>
Plain	71	105	39
$N = 1$	59 / 62	77 / 79	38 / 38
$N = 2$	41 / 52	45 / 45	37 / 37
$N = 4$	24 / 28	39 / 39	34 / 35

uration with  $N = 4$  dishes in parallel, avoiding 63%, 63%, and 13% CO<sub>2</sub> emissions with respect to the baseline.

Finally, because the decision-making algorithm applied in this work is purely temperature-based, these new insights are exclusively informative, but as previously commented, it opens a route to minimize important alternative aspects such as the ROI of the proposed system or the CO<sub>2</sub> removal (CDR).

## 5. Conclusions

The unsteady performance of the combined CSP-TES solution that provides a constant high temperature heat has been analyzed numerically in this work aimed at decarbonizing a given industrial activity (e.g. concrete, glass, chemicals, etc.) in two reference locations of southern Spain: Córdoba and Málaga, on the days March 22<sup>nd</sup>, June 22<sup>nd</sup> and December 22<sup>nd</sup> (i.e. two solstices and one equinox). To this end, the influence of a single solar dish or multiple dishes in parallel connection together with the size of the TES unit have been evaluated through a sensitivity anal-

ysis considering two main dimensionless parameters, namely the number of dishes  $N$  and the TES aspect ratio  $L/D$ . The results have shown that the configuration  $L/D = 1$  (in Córdoba) or  $L/D = 1.5$  (in Málaga) is that providing the maximum reduction of the additional external energy required to ensure the demanding heat of 27 kW at 800 °C ( $\simeq 650$  kWh).

On the other hand, considering that the TES unit is uniformly charged at the waste temperature at the cycle start, a simple decision-making algorithm has been implemented to analyze unsteady operation, dealing with charge, discharge or bypass strategies. In general, it has been shown that the TES unit plays a role in the system when the solar-dish outlet temperature exceeds that of the reference, e.g. on March 22<sup>nd</sup> and on June 22<sup>nd</sup> with  $L/D = 1.5$  and  $N \geq 2$ , in Córdoba. The results are very similar to those in Málaga, except for the case on March 22<sup>nd</sup> with  $N = 2$  and  $L/D = 1.0$ , where no TES operation takes place. Although the applied strategy seems reasonable, there are some cases in which the TES unit is not fully discharged at the end of the day, resulting

in a waste of energy. This fact motivates further studies to consider several consecutive days for the TES sizing. Alternatively, because the waste temperature and that of the demand could change depending on the industrial activity, a sensitivity analysis ranging along different values could result of interest to characterize the performance of the proposed system.

In economic terms, the impact of the CSP-TES has been analyzed assuming that the additional energy to meet the heat demand is accomplished by means of electric energy from the Spanish grid. This study has shown that although the electric price on December 22<sup>nd</sup> was extremely low due to renewable energy production, the use of the CSP-TES system has resulted in savings of up to a 33% with one dish, a 66% with two, and a 69% with four dishes, compared to the case operating with only electrical energy.

Additionally, the CO<sub>2</sub> footprint has also been investigated by means of the emissions derived from electric energy generation in the Spanish grid. Simulations have shown that the CO<sub>2</sub> removal is considerable, emitting up to 28, 60, and 66 fewer equivalent kg with respect to the baseline case.

In summary, the evaluation of the proposed CSP-TES system has revealed suitability for practical implementation, considering both energetic, economic and environmental aspects. It has been shown that the role of the TES with appropriate

control logic is essential for the system operation. Moving forward, further research could focus on refining the TES sizing methodology and exploring adaptive control strategies to optimize system performance under varying operational conditions.

## Appendix A. Validation

### *Appendix A.1. Solar dish*

The solar dish model in Eqs. (1) to (9) has been validated against the experimental measurements of Zhu et al. [8] in Table A.3. In terms of thermal efficiency Eq. (19), the solar dish model implemented in this study provided  $\eta = 81.27\%$ , which is quite in agreement with the experimental measurements of Zhu et al. [8] (81.5%), at the same mass flow rate  $\dot{m} = 0.043$  kg/s. Efficiency was obtained from the heat losses depicted in Fig. A.10, computed by means of Eqs. (12) to (17).

Note that the results depicted in Fig. A.10 may differ slightly from those of Zhu et al. [8] due to the different thermal coefficients adopted in each work. However, the trend in heat power losses is similar and the global efficiency is below 0.3 % with respect to the experiments.

### *Appendix A.2. Thermal Energy Storage (TES)*

As in previous studies [12, 14, 15, 36, 45], the validation of Eqs. (20) to (24) has been carried out against the experimental results of the thermocline tank pilot at Sandia National Laboratories [40], and with those of [22, 46], resulting

Table A.3: Validation of the numerical results provided by the solar dish model in Eqs. (1) to (8).

$T$ ( $^{\circ}\text{C}$ )	Num.	Ref.[8]
$T_i$	56.00	—
$T_1$	77.08	77.0
$T_2$	99.17	90.9
$T_3$	107.51	97.0
$T_4$	478.44	495.8
$T_f$	585.95	300.5
$T_w$	389.68	257.6
$T_{gi}$	404.34	233.1
$T_{go}$	354.11	
$T_o$	453.16	$\sim 450$

a good agreement in both cases. The choice of  $\Delta t = 3.6$  s and  $\Delta x = 1.2$  cm [14, 36] was in reasonable agreement with the reference, as shown in

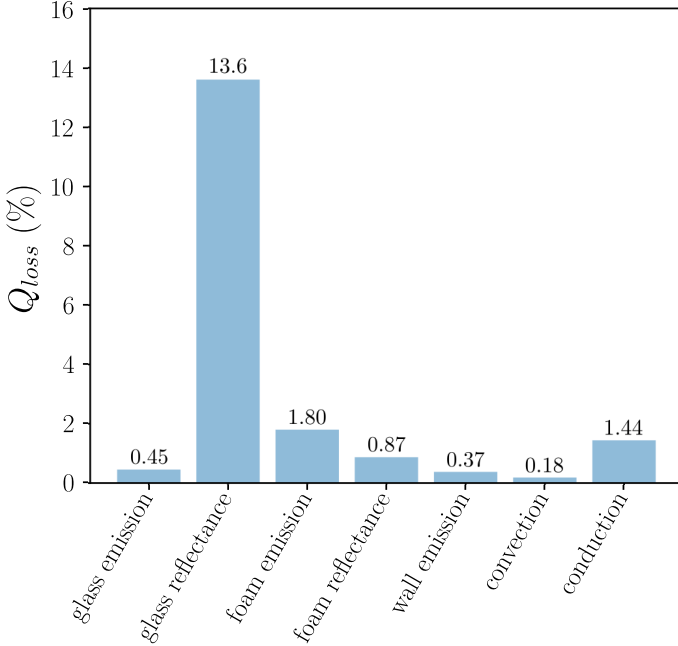


Figure A.10: Thermal losses in the validation case [8] computed with the current model of the solar dish.

Fig. A.11. The CFL condition ( $u\Delta t/\Delta x$ ) resulting from this configuration is maintained below 1, which ensures the stability of the simulations [37].

The thermophysical properties of the molten salts and quartzite [14, 43], and air [47] and rock [46] adopted in the simulations are shown in Table A.4.

### Appendix A.3. Glass window radiative balance

The high concentration ratio of solar radiation entering the receiver along with the volumetric absorption effects taking into account the thickness of the glass window  $L_g$ , makes it interesting to model this phenomenon. It implies the use of two different temperature values on both sides or borders of the glass window:  $T_{g,i}$  and  $T_{g,o}$  and the volumetric source term, which is defined based on the assumption that all visible radiation  $\dot{q}_v$  absorbed by the glass windows is homogeneously distributed throughout its volume. Only the direct concentrated solar beam  $I_b$  together with that reflected by the foam has been approximated as follows.

$$\dot{q}_v = \frac{\alpha_g I_b + \tau_g I_b F_{fg} \rho_f}{L_g}. \quad (\text{A.1})$$

This source term acts as an internal volumetric generation term within the glass domain to solve the 1D diffusion equation, based on a local coordinate system  $\hat{x}$  and constant thermal conductivity  $k_g = 1.4$  W m $^{-1}$  K $^{-1}$  of the medium,

$$T(\hat{x}) = -\frac{\dot{q}_v \hat{x}^2}{2k} + \left[ \frac{T_{gi} - T_{go}}{L_g} + \frac{\dot{q}_v L_g}{2k_g} \right] \hat{x} + T_{go}. \quad (\text{A.2})$$

Table A.4: Thermophysical properties of the HTF and of the packed bed material (temperatures in K where needed).

Solar salt	$\rho_f$	$\text{kg m}^{-3}$	$2090 - 0.636 T$
	$Cp_f$	$\text{J kg}^{-1} \text{ m}^{-1}$	$1443 + 0.172 T$
	$k_f$	$\text{W m}^{-1} \text{ K}^{-1}$	$0.443 + 1.9 \times 10^{-4} T$
	$\mu_f$	$\text{Pa s}$	$(22.174 - 0.12 T + 2.281 \times 10^{-4} T^2 - 1.471 \times 10^{-7} T^3)/1000$
Quartzite rocks	$\rho_s$	$\text{kg m}^{-3}$	2640
	$Cp_s$	$\text{J kg}^{-1} \text{ m}^{-1}$	1050
	$k_s$	$\text{W m}^{-1} \text{ K}^{-1}$	2.5
Compressed air (5 bar)	$\rho_a$	$\text{kg m}^{-3}$	15.4
	$Cp_a$	$\text{J kg}^{-1} \text{ m}^{-1}$	1032
	$k_a$	$\text{W m}^{-1} \text{ K}^{-1}$	0.037
	$\mu_a$	$\text{Pa s}$	$2.53 \times 10^{-5}$
Rock	$\rho_r$	$\text{kg m}^{-3}$	2560
	$Cp_r$	$\text{J kg}^{-1} \text{ m}^{-1}$	960
	$k_r$	$\text{W m}^{-1} \text{ K}^{-1}$	0.48



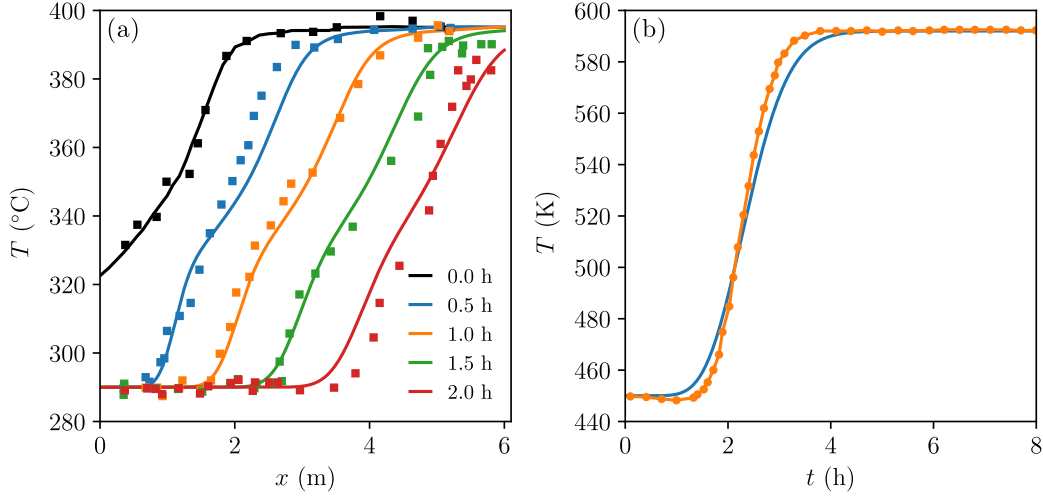


Figure A.11: Comparison of the numerical results (solid lines) with the experimental data from Sandia Laboratory pilot for molten salts [40] (a), and with the results of [22, 46] (b) for air flowing through a rocks packed-bed tank. Thermophysical properties are given in Table A.4.

From the temperature profile  $T(\hat{x})$  across the glass window and Fourier's Law, heat transferred at each border can be defined,

$$\dot{q}_{g,o} = k_g \frac{T_{g,o} - T_{g,i}}{L_g} - \frac{q_v L_g}{2} \quad (\text{A.3})$$

$$\dot{q}_{g,i} = k_g \frac{T_{g,o} - T_{g,i}}{L_g} + \frac{q_v L_g}{2} = q_v L_g + \dot{q}_{g,o}. \quad (\text{A.4})$$

## References

- [1] European Commission, COMMUNICATION FROM THE COMMISSION TO THE EUROPEAN PARLIAMENT, THE EUROPEAN COUNCIL, THE COUNCIL, THE EUROPEAN ECONOMIC AND SOCIAL COMMITTEE AND THE COMMITTEE OF THE REGIONS - RE-PowerEU Plan - COM(2022) 230 final, 2022. URL: <https://eur-lex.europa.eu/legal-content/EN/TXT/?uri=COM%3A2022%3A230%3AFIN>.
- [2] Directorate-General for Energy (European Commission), EU energy in figures - STATISTICAL POCKETBOOK, 2023. URL: <https://op.europa.eu/en/publication-detail/-/publication/bb9f16ee-642f-11ee-9220-01aa75ed71a1>.
- [3] S. Madeddu, F. Ueckerdt, M. Pehl, J. Peterseim, M. Lord, K. A. Kumar, C. Krüger, G. Luderer, The co2 reduction potential for the european industry via direct electrification of heat supply (power-to-heat), Environmental Research Letters 15 (2020) 124004.
- [4] X. Ma, Y. Du, B. Lei, Y. Wu, Energy, exergy, economic, and environmental analysis of a high-temperature heat pump steam system, International Journal of Refrigeration (2024).
- [5] Red Eléctrica, Informe del Sistema Eléctrico - Informe resumen de energías renovables 2022, 2023. URL: [https://www.sistemaelectrico-ree.es/sites/default/files/2023-03/Informe\\_Renovables\\_2022.pdf](https://www.sistemaelectrico-ree.es/sites/default/files/2023-03/Informe_Renovables_2022.pdf).
- [6] I. Heras-Saizarbitoria, E. Cilleruelo, I. Zamanillo, Public acceptance of renewables and the media: an analysis of the spanish pv solar experience, Renewable and Sustainable Energy Reviews 15 (2011) 4685–4696.
- [7] J. Coventry, C. Andraka, Dish systems for csp, Solar

- Energy 152 (2017) 140–170.
- [8] J. Zhu, K. Wang, Z. Jiang, B. Zhua, H. Wu, Modeling of heat transfer for energy efficiency prediction of solar receivers, *Energy* 190 (2020) 116372.
- [9] J. García Ferrero, R. Merchán, M. Santos, A. Medina, A. C. Hernández, P. Canhoto, A. Giostri, Modeling a solar pressurized volumetric receiver integrated in a parabolic dish: Off-design heat transfers, temperatures, and efficiencies, *Energy Conversion and Management* 293 (2023) 117436.
- [10] International Renewable Energy Agency, Innovation Outlook: Thermal Energy Storage, 2020. URL: [https://www.irena.org/-/media/Files/IRENA/Agency/Publication/2020/Nov/IRENA\\_Innovation\\_Outlook\\_TES\\_2020.pdf?rev=6950b7b9792344b5ab28d58e18209926](https://www.irena.org/-/media/Files/IRENA/Agency/Publication/2020/Nov/IRENA_Innovation_Outlook_TES_2020.pdf?rev=6950b7b9792344b5ab28d58e18209926).
- [11] S. Pascual, P. Lisbona, L. M. Romeo, Thermal energy storage in concentrating solar power plants: A review of european and north american r&d projects, *Energies* 15 (2022) 8570.
- [12] A. Abánades, J. Rodríguez-Martín, J. Roncal, A. Caraballo, F. Galindo, Proposal of a thermocline molten salt storage tank for district heating and cooling, *Applied Thermal Engineering* 218 (2023) 119309.
- [13] K. E. Elfeky, A. G. Mohammed, N. Ahmed, Q. Wang, Thermo-mechanical investigation of the multi-layer thermocline tank for parabolic trough power plants, *Energy* 268 (2023) 126749.
- [14] S. M. Flueckiger, B. D. Iverson, S. V. Garimella, J. E. Pacheco, System-level simulation of a solar power tower plant with thermocline thermal energy storage, *Applied Energy* 113 (2014) 86–96.
- [15] J.-F. Hoffmann, T. Fasquelle, V. Goetz, X. Py, A thermocline thermal energy storage system with filler materials for concentrated solar power plants: Experimental data and numerical model sensitivity to different experimental tank scales, *Applied Thermal Engineering* 100 (2016) 753–761.
- [16] F. Herbingier, M. Bhourri, D. Groulx, Investigation of heat transfer inside a pcm-air heat exchanger: a numerical parametric study, *Heat and Mass Transfer* 54 (2018) 2433–2442.
- [17] Y. Dutil, D. R. Rousse, N. B. Salah, S. Lassue, L. Zalewski, A review on phase-change materials: Mathematical modeling and simulations, *Renewable and sustainable Energy reviews* 15 (2011) 112–130.
- [18] M. A. Izquierdo-Barrientos, C. Sobrino, J. A. Almendros-Ibáñez, Thermal energy storage in a fluidized bed of pcm, *Chemical Engineering Journal* 230 (2013) 573–583.
- [19] A. Tiddens, M. Röger, H. Stadler, B. Hoffschmidt, Air return ratio measurements at the solar tower jülich using a tracer gas method, *Solar Energy* 146 (2017) 351–358.
- [20] E. E. John, W. M. Hale, R. P. Selvam, Development of a high-performance concrete to store thermal energy for concentrating solar power plants, volume 54686, 2011.
- [21] E. Villarroel, C. Fernandez-Pello, J. Lenartz, K. Parysek, High efficiency thermal storage system for solar plants (HELSOLAR). Final report, Technical Report, SENER Engineering and Systems, Inc., San Francisco, CA (United States); Univ . . . , 2013.
- [22] M. Hänchen, S. Brückner, A. Steinfeld, High-temperature thermal storage using a packed bed of rocks—heat transfer analysis and experimental validation, *Applied Thermal Engineering* 31 (2011) 1798–1806.
- [23] R. Mei, Carbon Dioxide Shuttling Thermochemical Storage Using Strontium Carbonate, Technical Report, Univ. of Florida, Gainesville, FL (United States), 2015.
- [24] A. Energy, Antora, 2020. URL: <https://antoraenergy.com/>.
- [25] MIT Technology Review, The hottest new climate technology is bricks, 2023. URL: <https://www.technologyreview.com/2023/01/11/1061111/the-hottest-new-climate-technology-is-bricks/>.

- [//technologyreview.com/2023/04/10/1071208/the-hottest-new-climate-technology-is-bricks/](https://technologyreview.com/2023/04/10/1071208/the-hottest-new-climate-technology-is-bricks/).
- [26] M. Papapetrou, G. Kosmadakis, A. Cipollina, U. La Commare, G. Micale, Industrial waste heat: Estimation of the technically available resource in the eu per industrial sector, temperature level and country, *Applied Thermal Engineering* 138 (2018) 207–216.
- [27] A. Inayat, Current progress of process integration for waste heat recovery in steel and iron industries, *Fuel* 338 (2023) 127237.
- [28] International Renewable Energy Agency, Innovation Landscape for smart electrification: Decarbonising end-use sectors with renewable power, 2023. URL: [https://mc-cd8320d4-36a1-40ac-83cc-3389-cdn-endpoint.azureedge.net/-/media/Files/IRENA/Agency/Publication/2023/Jun/IRENA\\_Innovation\\_landscape\\_for\\_smart\\_electrification\\_2023.pdf?rev=b92a90a778df450ea79ee8527ac1e334](https://mc-cd8320d4-36a1-40ac-83cc-3389-cdn-endpoint.azureedge.net/-/media/Files/IRENA/Agency/Publication/2023/Jun/IRENA_Innovation_landscape_for_smart_electrification_2023.pdf?rev=b92a90a778df450ea79ee8527ac1e334).
- [29] L. Migliari, S. Arena, P. Puddu, D. Cocco, Thermo-fluid dynamic analysis of a csp solar field line during transient operation, *Energy Procedia* 101 (2016) 1167–1174.
- [30] A. Cengel, *Heat transfer*, New York: McGraw-Hill, 2003.
- [31] A. Žukauskas, Heat transfer from tubes in crossflow, in: *Advances in heat transfer*, volume 8, Elsevier, 1972, pp. 93–160.
- [32] C. Zhao, T. Kim, T. Lu, H. Hodson, Thermal transport in high porosity cellular metal foams, *Journal of Thermophysics and Heat Transfer* 18 (2004) 309–317.
- [33] J. J. Moré, B. S. Garbow, K. E. Hillstrom, User guide for MINPACK-1, Technical Report, CM-P00068642, 1980.
- [34] P. Virtanen, R. Gommers, T. E. Oliphant, M. Haberland, T. Reddy, D. Cournapeau, E. Burovski, P. Peterson, W. Weckesser, J. Bright, S. J. van der Walt, M. Brett, J. Wilson, K. J. Millman, N. Mayorov, A. R. J. Nelson, E. Jones, R. Kern, E. Larson, C. J. Carey, Í. Polat, Y. Feng, E. W. Moore, J. VanderPlas, D. Laxalde, J. Perktold, R. Cimrman, I. Henriksen, E. A. Quintero, C. R. Harris, A. M. Archibald, A. H. Ribeiro, F. Pedregosa, P. van Mulbregt, SciPy 1.0 Contributors, SciPy 1.0: Fundamental Algorithms for Scientific Computing in Python, *Nature Methods* 17 (2020) 261–272. doi:10.1038/s41592-019-0686-2.
- [35] T. E. Schumann, Heat transfer: a liquid flowing through a porous prism, *Journal of the Franklin Institute* 208 (1929) 405–416.
- [36] K. Niedermeier, L. Marocco, J. Flesch, G. Mohan, J. Coventry, T. Wetzel, Performance of molten sodium vs. molten salts in a packed bed thermal energy storage, *Applied Thermal Engineering* 141 (2018) 368–377.
- [37] J. H. Ferziger, M. Perić, R. L. Street, *Computational methods for fluid dynamics*, springer, 2019.
- [38] C. R. Harris, K. J. Millman, S. J. van der Walt, R. Gommers, P. Virtanen, D. Cournapeau, E. Wieser, J. Taylor, S. Berg, N. J. Smith, R. Kern, M. Picus, S. Hoyer, M. H. van Kerkwijk, M. Brett, A. Haldane, J. F. del Río, M. Wiebe, P. Peterson, P. Gérard-Marchant, K. Sheppard, T. Reddy, W. Weckesser, H. Abbasi, C. Gohlke, T. E. Oliphant, Array programming with NumPy, *Nature* 585 (2020) 357–362. URL: <https://doi.org/10.1038/s41586-020-2649-2>. doi:10.1038/s41586-020-2649-2.
- [39] A. Butland, R. Maddison, The specific heat of graphite: An evaluation of measurements, *Journal of Nuclear Materials* 49 (1973) 45–56.
- [40] J. E. Pacheco, S. K. Showalter, W. J. Kolb, Development of a molten-salt thermocline thermal storage system for parabolic trough plants, *J. Sol. Energy Eng.* 124 (2002) 153–159.
- [41] P. W. Bridgman, *Dimensional analysis*, Yale univer-

sity press, 1922.

- [42] A. Martín-Alcántara, J. L. Aranda-Hidalgo, A. Jiménez-Solano, A. J. Sarsa-Rubio, Analysis and design of an inverted oscillating water column for energy storage under choked flow conditions, *Energy* 285 (2023) 129356.
- [43] J. T. Van Lew, P. Li, C. L. Chan, W. Karaki, J. Stephens, Analysis of heat storage and delivery of a thermocline tank having solid filler material (2011).
- [44] Red Eléctrica Española, REE, 2024. URL: <https://demanda.ree.es>.
- [45] A. Modi, C. D. Perez-Segarra, Thermocline thermal storage systems for concentrated solar power plants: One-dimensional numerical model and comparative analysis, *Solar Energy* 100 (2014) 84–93.
- [46] H. Peng, R. Li, X. Ling, H. Dong, Modeling on heat storage performance of compressed air in a packed bed system, *Applied energy* 160 (2015) 1–9.
- [47] I. H. Bell, J. Wronski, S. Quoilin, V. Lemort, Pure and pseudo-pure fluid thermophysical property evaluation and the open-source thermophysical property library coolprop, *Industrial & Engineering Chemistry Research* 53 (2014) 2498–2508. URL: <http://pubs.acs.org/doi/abs/10.1021/ie4033999>. doi:10.1021/ie4033999. arXiv:<http://pubs.acs.org/doi/pdf/10.1021/ie4033999>.